The Astronomical Journal, 170:196 (12pp), 2025 October https://doi.org/10.3847/1538-3881/adf637

When the Wall Fell: Study of Polycyclic Aromatic Hydrocarbons in T Chamaeleontis Using JWST

R. Arun
Indian Institute of Astrophysics, Sarjapur Road, Koramangala, Bangalore 560034, India; arunroyon@gmail.com
Received 2025 April 4; revised 2025 July 28; accepted 2025 July 29; published 2025 September 2

Abstract

We investigate the polycyclic aromatic hydrocarbon (PAH) emission features of T Cha, a G8-type T Tauri star that has exhibited "seesaw"-type mid-infrared continuum variability over nearly two decades due to the destruction of the disk's inner wall, using JWST/Mid-Infrared Instrument and Spitzer observations. We report the first detection of weak PAH emission at 6.2, 7.7, and 8.6 μm in the Spitzer/Infrared Spectrograph spectrum from 2005. The destruction of the inner wall in the 2022 JWST epoch allowed more ultraviolet photons to reach the outer disk, increasing the flux levels of PAH bands and allowing their detection well above the continuum. The 11.2 μm PAH flux increases by a factor of 3, yet its profile shape remains remarkably stable, and the 6.2/11.2 μm flux ratio has increased, but the charge state of the PAH population remains 75% neutral. The PAH features exhibit a "class C" spectral profile, with redshifted peaks and broadened wings consistent with emission from low-mass T Tauri disks, while the weak 12.7/11.2 ratio points to a lower abundance of duo and trio hydrogen modes, implying a predominantly zigzag carbon structure. A faint "class A" subcomponent in the 6.2 and 7.7 μm bands may indicate additional PAH processing by ultraviolet radiation from accretion hotspots. Placement on PAH charge–size grids locates T Cha in the low-ionization, small-size regime ($N_C \leqslant 30$), signifying a largely neutral PAH population in multiple epochs spanning 18 yr. Through multiepoch, high-resolution data from JWST and Spitzer, we identify T Cha as a benchmark source for probing disk evolution and PAH processing, emphasizing the potential of temporal monitoring with JWST.

Unified Astronomy Thesaurus concepts: Astrochemistry (75); Herbig Ae/Be stars (723); Polycyclic aromatic hydrocarbons (1280); Protoplanetary disks (1300); T Tauri stars (1681); Young stellar objects (1834)

1. Introduction

Transitional disks, which are characterized by large dust cavities and low near-infrared excess, represent an essential evolutionary stage between optically thick protoplanetary disks and dispersed systems (see C. Espaillat et al. 2014). They have drawn considerable interest because they can exhibit diverse clearing mechanisms, such as photoevaporation, planet–disk interactions, and disk winds (J. E. Owen 2016; B. Ercolano & I. Pascucci 2017). Over the past two decades, multiwavelength observations have revealed that some transitional disks show high levels of temporal variability in their infrared continuum (J. Muzerolle et al. 2009; C. Espaillat et al. 2011; K. Flaherty et al. 2012). This variability can offer unique windows into disk dynamics close to the star, including phenomena such as changes in the inner disk wall or fluctuations in accretion rates.

Within this framework, T Cha has emerged as an intriguing and well-studied example. T Cha is a young (2–10 Myr; D. Fernández et al. 2008), accreting ($\sim 6 \times 10^{-9}$ $M_\odot$ yr^{-1}; E. Cahill et al. 2019) G-type star surrounded by a disk containing a substantial inner gap (from ~0.2 to 10 au), which has been imaged through near-infrared interferometry and millimeter observations (J. Olofsson et al. 2013; N. Huélamo et al. 2015; A. Pohl et al. 2017). The system exhibits large-amplitude optical variability, including episodic outbursts, and has displayed a pronounced "seesaw" signature, which refers to an inverse change in the mid-infrared (mid-IR) continuum at short and long wavelengths, on multiyear timescales (E. Schisano et al. 2009; E. Cahill et al. 2019).

Using the James Webb Space Telescope (JWST) and archival Spitzer data, combined with optical and infrared photometric variability, C. Xie et al. (2025) studied this seesaw effect in T Cha. Their study shows that between the earlier Spitzer data and more recent JWST/Mid-Infrared Instrument (MIRI) observations, the flux at shorter mid-IR wavelengths (roughly 5–10 μm) decreased, whereas the flux at longer mid-IR wavelengths (beyond about 15 μm) increased. This flip in flux, where one wavelength region goes down while another goes up, resembles the two ends of a seesaw moving in opposite directions (J. Muzerolle et al. 2009; C. C. Espaillat et al. 2024). In T Cha, C. Xie et al. (2025) interpret this behavior as a result of changes in the geometry of the inner disk: as the inner dust wall becomes less tall or less massive, more radiation reaches the outer or shadowed disk, enhancing longer-wavelength emission. Conversely, as the inner wall is destroyed, near- and mid-IR emission from the innermost dust decreases, leading to a dip in the short-wavelength mid-IR range but a rise in the longer-wavelength mid-IR.

Earlier mid-IR spectra acquired with Spitzer suggested the presence of 11.2 μm polycyclic aromatic hydrocarbons (PAHs; V. C. Geers et al. 2006), indicating that ultraviolet (UV) photons from the star penetrate regions of the disk's surface layer. More recently, N. S. Bajaj et al. (2024) reported that the JWST spectra show 6.2, 7.7, and 8.6 μm PAH features, which were not previously reported in the older Spitzer data. PAHs serve as tracers of UV radiation and are sensitive to the physical conditions in the disk's upper layers (V. C. Geers

Table 1
Observation Log for Mid-IR Spectra of T Cha Used in the Study

Mission/Instrument	Observation Date	Proposal ID/Astronomical Observation Request (AOR)	PI
Spitzer/IRS	2004 Jul 18	5641216	N. Evans
Spitzer/IRS	2005 May 30	12679424	J. R. Houck
VLT/ISAAC (*L* band)	2006 Apr 18	⋯	G. Geers
JWST/MIRI MRS	2022 Aug 13–14	2260	I. Pascucci

et al. 2006; A. G. G. M. Tielens 2011). Their emission profiles are often grouped into classification schemes, commonly referred to as classes A, B, C, and D—based on band peak positions and shapes (E. Peeters et al. 2002; B. van Diedenhoven et al. 2004; M. Matsuura et al. 2014).

UV photons excite the PAH molecule, which then relaxes through various vibrational modes and produces the infrared features that show up in the astrophysical spectra. The near-IR PAH feature in the 3.3 μm region is due to the C–H stretching mode. The 6.2 and 7.7 μm band features are attributed to C–C stretch modes (A. G. G. M. Tielens 2008), and they shift systematically to the redder wavelengths in different environments. In class A sources (H II regions, reflection nebulae) they peak at 6.22–6.25 and 7.6 μm. Class B spectra (planetary nebulae, Herbig Ae/Be stars) move to 6.25–6.28 and 7.8 μm, whereas class C spectra from cool T Tauri disks peak at 6.28–6.30 μm and exceed 8 μm. The 8.6 μm line traces C–H in-plane bending modes (E. Peeters et al. 2002; B. van Diedenhoven et al. 2004). The 11.2 μm band arises from solo C–H out-of-plane bends in large, neutral PAHs; its weaker 11.0 μm companion comes from cations, so their ratio traces ionization (E. Peeters et al. 2002). The 12.7 μm band stems from trio (and minor duo) C–H out-of-plane bends (A. G. G. M. Tielens 2008).

In this paper, we use the JWST/MIRI Medium Resolution Spectrometer (MRS) and Spitzer spectra of T Cha to study the continuum and PAH variability and characterize the newly identified PAH bands. In Section 2, we describe the observational details of Spitzer, JWST, and Very Large Telescope (VLT)/ISSAC data sets. Section 3, describes the analysis and results, and is followed by a brief discussion of UV hardness and PAH charge and size in Section 4. We conclude with a summary of the work with a future scope in Section 5.

2. Observations and Data Reduction

The study is based on three archival mid-IR spectra from Spitzer, VLT/ISAAC, and JWST spanning nearly two decades. The first data set is of archival Spitzer Infrared Spectrograph (IRS) short high (SH) and long high (LH) observations from 2004 (V. C. Geers et al. 2006), which provided the earliest high-quality view of T Cha's mid-IR emission. The second data set consists of short low (SL) and long low (LL) observation along with SH+LH spectra observed in 2005 (J. M. Brown et al. 2007). The SH and LH spectra in 2005 are noisy, thus we use the SL mode for the work. We retrieved these data from the enhanced offline version of the Combined Atlas of Sources with Spitzer IRS Spectra (CASSIS[1]) archive (V. Lebouteiller et al. 2011, 2015), CASSISjuice (V. Lebouteiller 2023). The spectral coverage included both the SH and LH modules, extending roughly from 10 to 35 μm at a resolving power of $R \approx 600$ in the high-resolution configuration or $R \approx 60$ in low-resolution mode, depending on the particular observation. Table 1 shows the details of observation.

The third data set is a newly acquired JWST/MIRI MRS observation obtained on 2022 August 13–14 as part of the Cycle 1 General Observer program (Proposal ID: 2260; PI: I. Pascucci). As reported by N. S. Bajaj et al. (2024) and A. D. Sellek et al. (2024), these observations totaled 3.24 hr on-source (4.48 hr including overheads) and covered the full range of the MIRI MRS from approximately 5 to 28 μm. The MRS operates in four channels, each divided into three subbands, yielding 12 individual spectral segments, which were subsequently stitched to form a single continuous spectrum at a resolving power of $R \sim 3000$. Detail of the reduction steps is given by N. S. Bajaj et al. (2024). The calibrated JWST/MIRI/MRS spectra offer a significantly improved sensitivity and spectral resolution over the Spitzer IRS data, enabling a comparative study of PAH variability.

The VLT/ISAAC *L*-band observations of T Cha on 2006 April 18 captured the 3.3 μm PAH feature (V. C. Geers et al. 2007), which is not covered at the JWST/MIRI and Spitzer wavelengths. Owing to the lack of JWST/NIRSpec data, this 3.3 μm feature is used in the study complementing the mid-IR PAH analysis from JWST.

3. Analysis and Results

3.1. Understanding the Variability in the Continuum Emission

To investigate the continuum evolution of T Cha, we compare the JWST/MIRI MRS spectrum (2022) with two archival Spitzer/IRS data sets obtained in 2004 and 2005. The Spitzer SH+LH data from 2004 are mentioned by C. Xie et al. (2025), but the focus is on the Spitzer SL spectrum from 2005, as the 2004 SH+LH data set is not directly comparable over the 5–15 μm range. We include the 2004 data set as an additional data point, as we are looking at the variability of PAHs in different epochs.

Figure 1 compares the JWST spectrum of T Cha (red line) with the archival Spitzer/IRS data taken in 2004 (blue line; SH module) and 2005 (black line; SL module). The 2004 SH data provide coverage at wavelengths above 10 μm, but clearly show the 11.2 μm PAH emission. There are several noteworthy differences: the flux level in the 5–10 μm range is substantially lower in the JWST spectrum than in either Spitzer data set, while at wavelengths longer than about 12–13 μm the JWST continuum rises relative to earlier epochs. This behavior exemplifies the "seesaw" effect reported by C. Xie et al. (2025), wherein the short-wavelength mid-IR flux decreases as the longer-wavelength emission increases. The 2004 and 2005 Spitzer data sets show a similar slope in the

[1] CASSIS is a product of the IRS instrument team, supported by NASA and JPL.

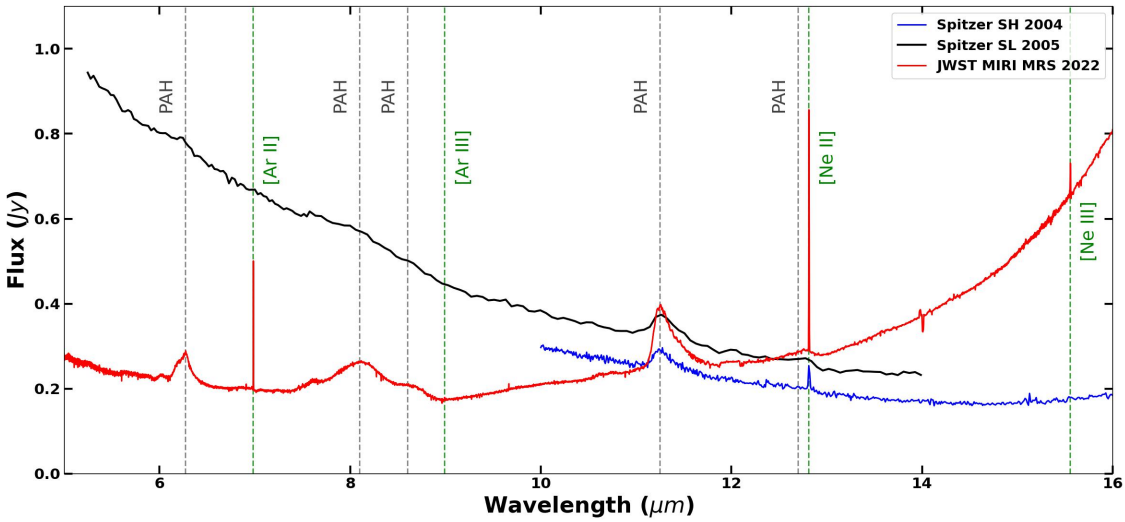

Figure 1. Comparison of the JWST/MIRI MRS spectrum of T Cha (red) with two Spitzer/IRS data sets: the 2004 SH module (blue) and the 2005 SL module (black). The 2005 data cover the 5–15 μm range, while the 2004 SH observation starts at 10 μm. The "seesaw" effect is evident, with the JWST continuum showing diminished flux below 10 μm but enhanced emission at longer wavelengths, compared to the 2005 Spitzer spectra. Forbidden lines ([Ar II], [Ar III], [Ne II], [Ne III]) and the main PAH bands are marked with vertical dashed lines.

continuum suggestive of similar disk structure. The higher flux in 2005 data over 2004 might be due to the larger aperture of Spitzer low-resolution data.

In the JWST/MIRI spectrum, all prominent PAH features previously not reported in the older Spitzer data are clearly observed, with the exception of the well-known 11.2 μm feature, which was already reported in earlier observations (V. C. Geers et al. 2006). Specifically, N. S. Bajaj et al. (2024) report PAH bands at 6.02 μm and 8.22 μm, as well as ubiquitous features at 6.2, 7.7, 8.6, 12.0, and 12.7 μm in the JWST data set, which were not reported by previous Spitzer studies. The study demonstrated that PAH emission is spatially extended, confirming it primarily traces the disk's illuminated surface layers. The clear detection of all PAH bands in the JWST epoch might be due to the diminished inner dust wall that permits more UV flux to reach the PAH-rich surface layers in the outer disk allowing conditions for increased excitation of PAHs (N. S. Bajaj et al. 2024; C. Xie et al. 2025). The higher sensitivity of JWST aided because it raised the signal-to-noise ratio of the PAH features.

The destruction of the wall and subsequent illumination of the outer disk give us a unique opportunity to study the PAH population in a transitional disk. In the following sections, we provide a comprehensive analysis of individual PAH bands, studying their variability in different epochs and comparing their properties with some reference young sources.

3.2. Processing of the Spectra

For further analysis and comparison, we process the all multiepoch spectra of T Cha. The processes of continuum subtraction and flux estimation of all spectra are described below.

3.2.1. Continuum Subtraction of the Spectra

To isolate the PAH emission features and for robust flux measurements across multiple epochs, we performed continuum subtraction using a cubic spline interpolation technique.

For the JWST and Spitzer/IRS SL spectra (5–15 μm region), we adopted continuum anchor points from J. Y. Seok & A. Li (2017) and R. Arun et al. (2023), optimized for PAH-dominated young stars. These include nodes at 5.55, 5.80, 6.70, 7.00, 9.15, 9.45, 9.70, 10.20, 10.70, 11.80, 12.20, 13.05, 13.25, 13.80, 14.00, and 14.80 μm.

For the higher-resolution SH spectrum (10–15 μm region), we used anchor points at 10.20, 10.70, 11.80, 12.20, 13.05, 14.00, and 14.99 μm. These intervals were selected to avoid known PAH bands and emission lines while preserving the integrity of the underlying continuum shape.

For the VLT/ISAAC spectra, we applied a continuum subtraction described by V. C. Geers et al. (2007). The continuum was modeled as a linear function fitted over selected anchor regions free of emission features. The anchor points were chosen around the target features, following the continuum intervals used in PAH studies (e.g., at 3.05–3.07, 3.10–3.70, 3.45–3.50, 3.667–3.689, and 3.7068–3.720 μm). Once the linear baseline was established, it was subtracted from the observed spectrum.

3.2.2. Gaussian Decomposition of the 6 μm PAH Complex

The analysis of PAH emission features is often enhanced by decomposing the spectral profiles into multiple Gaussian components. Following the methodology of E. Peeters et al. (2024), who modeled the 3 μm PAH region using ten Gaussians (nine distinct PAH bands and one underlying plateau), we similarly performed a multicomponent Gaussian decomposition of the 6 μm PAH region. This region was fit with six Gaussian profiles (C1–C6). During the fitting process, the central wavelength of each Gaussian component was constrained to lie within $\pm$0.025 μm of its nominal position, and the FWHM values were restricted to $\pm$0.0025 μm. This decomposition allows for the identification and separation of the 6.0 μm feature, which is potentially associated with C=O (carbonyl) stretching vibrations (E. Peeters et al. 2002) or olefinic C=C bonds (C.-H. Hsia et al. 2016), and also separation from other PAH subcomponents. To examine the detailed substructure of the 6 μm PAH complex in T Cha, we

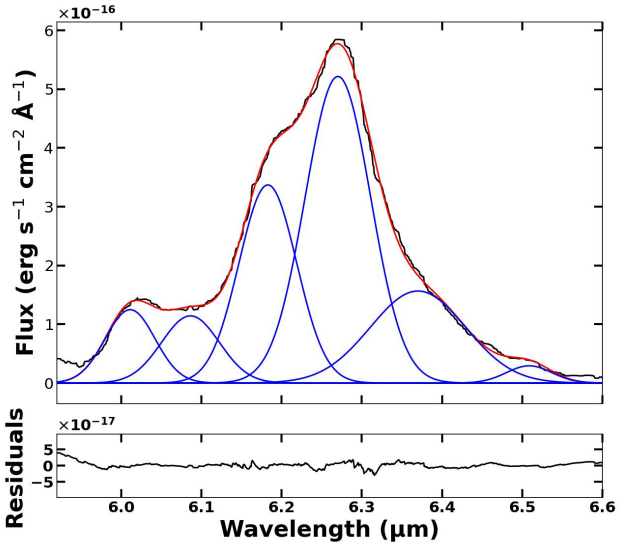

Figure 2. Gaussian decomposition of the 6 μm PAH emission in T Cha. The median-filtered spectrum is shown in black. The colored lines indicate individual Gaussian components, and the red line marks the total fitted model. The lower panel plots residuals (data minus model). The primary emission peak at 6.273 μm is significantly shifted relative to the more commonly reported 6.2 μm feature, characteristic of border class B/class C PAH spectra.

first performed median filtering on the continuum-subtracted spectrum to mitigate narrow emission spikes and instrumental artifacts. Specifically, we employed a median filter with a kernel size of 31 data points, which effectively suppresses sharp features while preserving the broad PAH emission. We then restricted our analysis to the wavelength range 5.95–6.55 μm, where the strongest PAH emission is expected in this system (see Figure 2).

The initial parameters of the Gaussian components are listed in Table A1 in Appendix A.

The multi-Gaussian fitting is performed using Levenberg–Marquardt minimization (LevMarLSQFitter) from *astropy* (Astropy Collaboration et al. 2022) to converge on the best-fit parameters for each Gaussian. We then numerically integrated each fitted component over wavelength to obtain its flux. Figure 2 shows the median-filtered data (black line), individual Gaussian components (blue), their sum (red line), and the residuals. In general, the fit reproduces the broad substructures of the 6 μm PAH complex well.

Table 2 lists the integrated flux of each fitted Gaussian component and the total PAH flux for T Cha's 5.95–6.55 μm region. We find that the strongest emission peaks near $\lambda \approx 6.27$ μm, consistent with border class B/class C type PAHs, which are frequently shifted to longer wavelengths than the 6.2 μm band of class A (e.g., E. Peeters et al. 2002). The combined flux from the 6 μm region is $\sim 1.29 \times 10^{-12}$ erg s^{-1} cm^{-2}.

3.2.3. Estimation of PAH Fluxes

We estimated the integrated fluxes of the 6.2, 7.7, 8.6, 11.2, and 12.7 μm PAH bands in the JWST spectrum of T Cha using direct numerical integration of the continuum-subtracted spectrum. The total flux of the 6.2 μm PAH feature (the sum of all six components) matches the integrated flux. The PAH features in T Cha are shifted due to their class C characteristics (discussed in the following sections); integration intervals are chosen accordingly to encompass the redward extension and

Table 2
Parameters and Integrated Fluxes from the Multi-Gaussian Fit of the 6 μm Region in T Cha, Rounded to Three Significant Figures

Component	Amplitude (erg s^{-1} cm^{-2} Å^{-1})	Mean (μm)	σ (μm)	Flux (erg s^{-1} cm^{-2})
C1	1.25×10^{-16}	6.01	0.031	9.68×10^{-14}
C2	1.14×10^{-16}	6.09	0.036	1.03×10^{-13}
C3	3.37×10^{-16}	6.18	0.036	3.04×10^{-13}
C4	5.21×10^{-16}	6.27	0.040	5.34×10^{-13}
C5	1.57×10^{-16}	6.37	0.060	2.33×10^{-13}
C6	2.93×10^{-17}	6.50	0.030	2.08×10^{-14}
		Total flux		1.29×10^{-12}

Table 3
Measured PAH Fluxes from the Mid-IR Spectra of T Cha

	PAH Feature (μm)	Flux (erg s^{-1} cm^{-2})
VLT/ISAAC	3.3	2.242×10^{-12}
Spitzer 2004	11.0 + 11.2	$(2.85 \pm 0.3) \times 10^{-13}$
	12.7[a]	$(6.30 \pm 0.1) \times 10^{-14}$
Spitzer 2005	Σ6.2	$(4.17 \pm 0.91) \times 10^{-13}$
	7.7	$(8.56 \pm 0.82) \times 10^{-13}$
	8.6	$(2.37 \pm 0.62) \times 10^{-13}$
	11.0 + 11.2	$(5.40 \pm 0.24) \times 10^{-13}$
	12.7[a]	$(0.41 \pm 0.28) \times 10^{-13}$
JWST	Σ6.2	$(1.27 \pm 0.01) \times 10^{-12}$
	7.7	$(2.75 \pm 0.004) \times 10^{-12}$
	8.6	$(4.79 \pm 0.03) \times 10^{-13}$
	11.0	$(3.34 \pm 0.10) \times 10^{-14}$
	11.2	$(9.15 \pm 0.02) \times 10^{-13}$
	12.7[a]	$(1.37 \pm 0.03) \times 10^{-13}$

Note.
[a] The 12.7 μm PAH flux is reported after subtraction of [Ne II] 12.81 μm line flux.

asymmetry typical of class C profiles. The 6.2 μm PAHs are integrated between 5.9 and 6.6 μm, similar to the range of Gaussian decomposition. The 7.7 μm complex was integrated between 7.0 and 8.45 μm and the 8.6 μm band over 8.45–9.05 μm. For the 11–13 μm region, we adopted 10.9–11.13 μm for the 11.0 μm band, 11.13–11.75 μm for the 11.2 μm band, and 12.2–13.1 μm for the 12.7 μm feature. The final flux of 12.7 μm is estimated after the subtraction of [Ne II] 12.81 μm line flux. The resulting fluxes are tabulated in Table 3. Figure B1 in Appendix B illustrates the flux integration of PAH features.

To estimate uncertainties on the integrated PAH fluxes, we employed a Monte Carlo approach similar to that used by N. S. Bajaj et al. (2024). First, we fit a linear baseline to continuum regions adjacent to each PAH feature and computed the standard deviation (σ) of the residuals between the observed spectrum and the fitted continuum in these regions. We then generated 5000 synthetic spectra by adding Gaussian noise with standard deviation σ to the observed continuum-subtracted flux. For each realization, we performed numerical integration over the same wavelength intervals used for the PAH features (as described above). The standard deviation of the resulting distribution of integrated flux values was adopted as the 1σ uncertainty on the measured PAH flux. This method

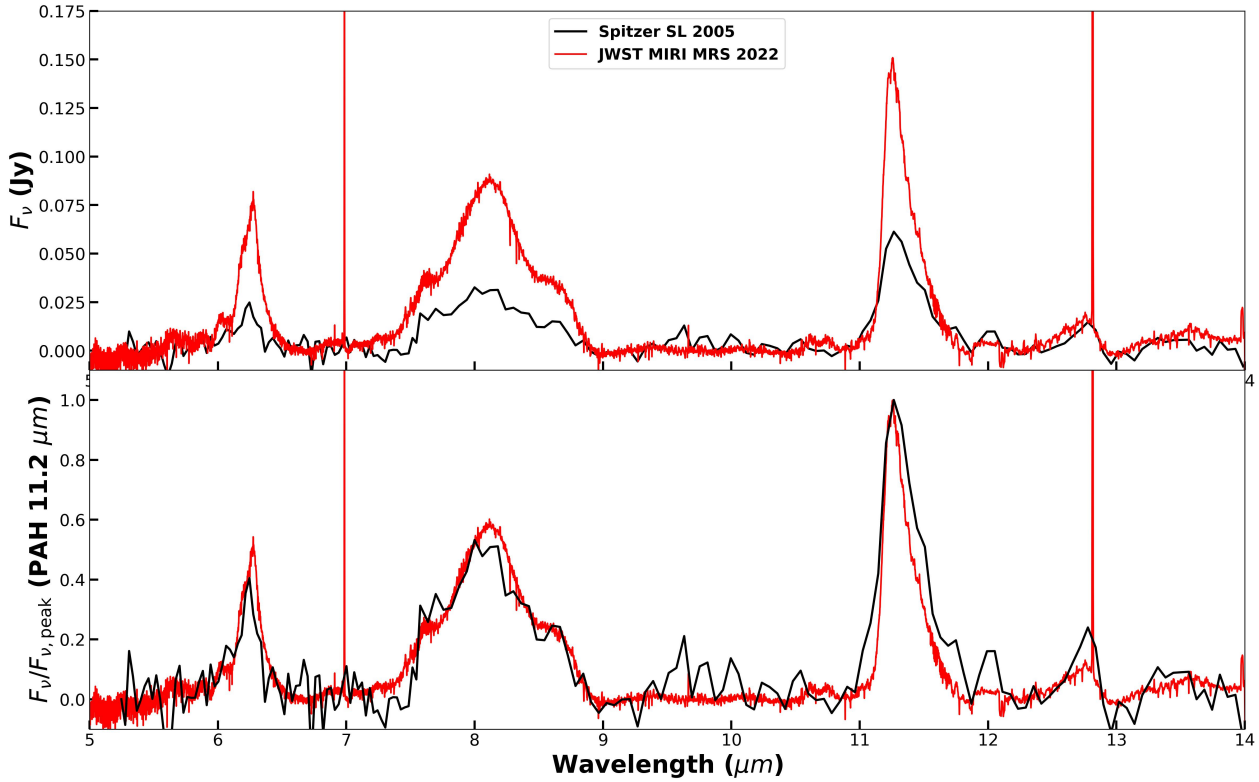

Figure 3. Continuum-subtracted mid-IR spectra of T Cha from JWST/MIRI (red) and archival Spitzer SL observations (black). Top panel: continuum-subtracted spectral comparison showing prominent emission features between 5 and 14 μm in both JWST and Spitzer. Bottom panel: same spectra normalized to the peak of the 11.2 μm PAH feature, emphasizing the ratios have not changed significantly over the 18 yr timescale.

accounts for both the spectral noise and the sensitivity of the flux integration to local continuum variations.

The flux estimation in continuum-subtracted Spitzer spectra (low and high resolution) follows a similar approach to that for JWST spectra above. The errors are estimated accounting for flux uncertainties given in CASSISJuice spectra (R. Arun et al. 2025). Due to the weak PAHs in Spitzer SL, we do not decompose the 6.0 and 6.2 μm features but integrate them to get composite flux in the wavelength range 5.9–6.5 μm. The other PAH features are integrated in the same regions as the JWST spectra. The fluxes are given in Table 3.

The continuum-subtracted VLT/ISAAC *L*-band spectrum is integrated between 3.28 and 3.40 μm to estimate the flux in the 3.3 μm PAH feature. The integration of the VLT/ISAAC *L*-band spectrum is shown in Figure B2.

3.3. PAHs in the Spitzer SL Spectrum

The Spitzer observation of T Cha in the high-resolution mode (AOR—5641216) taken in 2004 has been used previously for various studies (J. Kessler-Silacci et al. 2006; J. M. Brown et al. 2007; V. C. Geers et al. 2007; F. Lahuis et al. 2007). But the low-resolution (SL: $R \sim 60$) Spitzer spectrum (AOR—12679424) has not been used by previous studies until recently. C. Xie et al. (2025) used the data for establishing the "seesaw effect," mentioning that the data are from J. M. Brown et al. (2007), but the data reported in the paper are the SH+LH mode. We found significant bumps at the PAH wavelengths in the spectrum, and we performed a continuum subtraction detailed in Section 3.2. We report for the first time a small but significant detection of PAHs in the 6.2, 7.5–9, and 11.2 μm regions in the Spitzer SL spectrum of T Cha from 2005.

The detection of PAHs in the Spitzer SL spectra gives us a unique opportunity to compare the flux ratios. We compared the continuum-subtracted Spitzer SL and JWST spectra of T Cha which are shown in Figure 3. The bottom panel shows the flux of both epochs normalized to the peak of 11.2 μm PAHs. Interestingly, the flux in the composite 11.2 μm PAH (11.0 + 11.2) feature has increased $\sim$1.75 times from the Spitzer SL epoch to the JWST epoch, indicative of the higher UV fluorescence due to destruction of the wall. The normalized figure (bottom panel) shows that the flux of the 6.2 μm PAH and the 7.7 μm complex relative to the 11.2 μm PAH does not show any significant change between epochs. The 6.2/11.2 PAH flux ratio is 0.77 ± 0.17 in the Spitzer epoch and 1.34 ± 0.04 in the JWST epoch. In the case of the 7.7/11.2 ratio, the values are 1.59 ± 0.17 and 2.9 ± 0.08, respectively. N. S. Bajaj et al. (2024) found that the flux ratios at the JWST epoch indicate a neutral PAH population in the T Cha disk. While both ratios nearly double, they stay in the low-ionization PAH regime. In our charge–size analysis (Section 4.2), based on the grids of A. Maragkoudakis et al. (2020), these ratios place T Cha at $\sim$75% neutral. For context, highly ionized PAH environments in disks typically exhibit substantially larger 7.7/11.2 ratios than observed for T Cha. The 7.7/11.2 ratio is 4.2, 6.2, and 11.0 for SR 21A, PDS 144N, and HD 97300, respectively, broadly increasing with stellar UV output (R. Arun et al. 2025).

The 7.7/11.2 ratio has increased slightly in the JWST epoch, which indicates a small increase in ionization (A. Maragkoudakis et al. 2020). But the increase does not

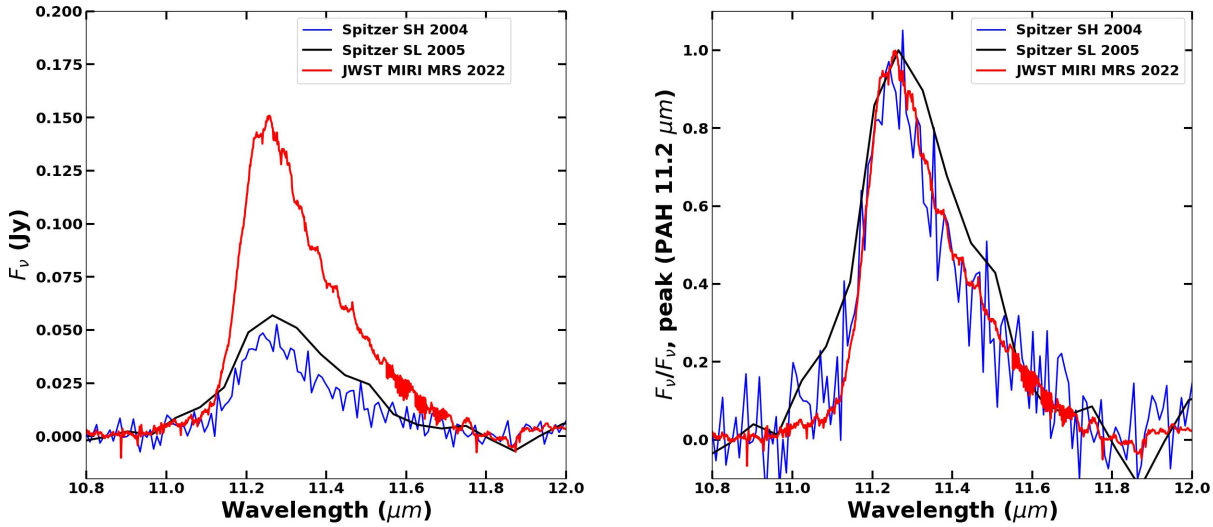

Figure 4. Comparison of the 11.2 μm PAH feature in T Cha's continuum-subtracted spectra from different epochs (left) and the 11.2 μm PAH feature normalized to its peak amplitude (right): Spitzer SH (blue) in 2004, Spitzer SL (black) in 2005, and JWST/MIRI (red) in 2022. Left: all spectra plotted in absolute flux units, revealing a factor of $\sim$3 increase in feature strength in the JWST epoch compared to the two Spitzer observations. Right: the same data normalized to the peak flux of the PAH feature, showing no appreciable change in profile shape.

alter the ionization of the PAH population significantly (further details are discussed in Section 4.2).

3.4. Variability of the 11.2 μm Feature

The 11.2 μm PAH band is among the most prominent PAH features in astrophysical environments (S. Hony et al. 2001; A. G. G. M. Tielens 2008). The shape of the PAH profile primarily traces PAH charge/size and the hardness of the radiation field (A. Maragkoudakis et al. 2020), but the band flux mainly tracks the intensity of the UV field. All three spectral epochs for T Cha show the 11.2 μm PAH feature. Given the noticeable variability in the continuum, likely due to changes in the inner wall structure, this offers a unique opportunity to investigate the variability in both the flux and profile shape of the 11.2 μm PAH feature in T Cha.

The two Spitzer epochs, which are separated by approximately one year, show small flux variation in the 11.2 μm feature, indicating similar disk structure. However, the JWST spectrum (Figure 4, left) reveals that the 11.2 μm band flux has increased by a factor of $\sim$3 compared to the Spitzer SH+LH measurements in 2004 and by a factor of $\sim$1.75 relative to the SL measurements in 2005. The estimated flux from JWST and 2005 Spitzer spectra matches estimates from N. S. Bajaj et al. (2024). The threefold increase in the 11.2 μm flux shows that the destruction of the inner disk wall (C. Xie et al. 2025) allowed additional exposure of the outer disk surface to the UV flux. This heightened UV exposure excites PAH molecules more efficiently, enhancing the flux of the feature (A. G. G. M. Tielens 2008).

The investigation of profile morphology also gives a similar conclusion. Despite the flux increase, normalizing the profiles at their peaks indicates that the shape of the 11.2 μm PAH band remains essentially unchanged across the three epochs (Figure 4). The profile of PAH features is influenced by environmental conditions such as ionization, grain size distribution, and radiation hardness (A. Maragkoudakis et al. 2020). The invariance in the 11.2 μm band shape indicates that the underlying PAH population remains largely unaffected by increasing UV intensity. This also suggests that variations in the UV field intensity (i.e., the number of photons) are not the primary driver of the changes in PAH feature profiles in various astrophysical environments. Instead, the variability may be attributed to the hardness of the UV field (i.e., change in λ). One caveat here is that, among the prominent PAH features, the profile of the 11.2 μm band is considered less sensitive to variations in the radiation field hardness and ionization state. Thus, even if there is a slight increase in hardness of photons due to enhanced accretion episodes in T Cha (E. Cahill et al. 2019), it is not great enough to affect the profile of the 11.2 μm PAH band. Future JWST follow-ups, while the inner wall persists, will be able to study the effects of radiation hardness on 6.2 and 7.7 μm PAH bands in T Cha system. Long-baseline photometry reveals recurrent wall-high/wall-low episodes on month-to-year timescales (C. Xie et al. 2025), suggesting that follow-ups can be scheduled by monitoring and triggering JWST during sustained "high" states.

The invariance of the 11.2 μm PAH profile (peak and FWHM) and the PAH ratios relative to 11.2 μm across epochs suggest that the PAH size distribution and ionization state remained largely unchanged despite the factor of $\sim$3 flux increase. The lack of peak shifts or broadening could indicate minimal processing (e.g., fragmentation) of large, neutral PAHs, which dominate the 11.2 μm emission in shielded disk regions (E. Peeters et al. 2002; C. W. Bauschlicher et al. 2008). Additionally, the absence of ionization signatures (e.g., the 11.0 μm feature attributed to the CH out-of-plane bending mode of lone hydrogen groups in PAH cations) supports a neutral charge state (A. G. G. M. Tielens 2008) consistent with the inference from N. S. Bajaj et al. (2024).

3.5. Comparing the PAH Feature with Reference Sources

To better understand the newly detected PAH emission features in the T Cha system in the JWST spectrum, we compared its continuum-subtracted spectrum with four reference sources that display strong PAH features: the

photodissociation region (PDR) template for the Orion H II region from JWST (hereafter "H II PDR"; R. Chown et al. 2024), the intermediate-mass star HD 97300 (B9) with associated nebulosity (P. Manoj et al. 2011), the Herbig Ae star PDS 144N (A2) with an edge-on disk with flare morphology (M. D. Perrin et al. 2006), and the T Tauri star SR 21A (G3; V. C. Geers et al. 2006). The JWST spectrum of the H II PDR is taken from R. Chown et al. (2024) released in the PDR4ALL[2] repository; for the remaining young stellar objects, the Spitzer spectra are taken from CASSISJuice. The Spitzer sources are selected for their broad range of stellar effective temperature ($T_{\rm eff}$) and availability of Spitzer observations of low- and high-resolution spectra along with strong PAH emission (R. Arun et al. 2025). To compare the PAH features in the T Cha spectrum with reference objects, all spectra were first continuum-subtracted using the spline-based method described in Section 3.2. The next part of this section uses the above data to compare PAHs in the spectra in various wavelength ranges.

3.5.1. 6.2 μm PAH

To compare the 6.2 μm PAH feature in the T Cha spectrum with reference objects, we aligned the spectra, dividing each by its respective 6.2 μm peak flux, effectively normalizing the peak of 6.2 μm feature to unity (i.e., $F_\nu/F_{\nu,\rm peak}$). The resulting scaled spectra illustrate the shift in peak position, asymmetries in the band wings, and contrast in the overall band shapes. Figure 5 (top panel) shows each spectrum centered on the 5.8–6.6 μm region.

In Section 3.2.2, we found that the 6.2 μm feature of T Cha (red line) peaks at ∼6.27 μm, and is shifted toward longer wavelengths relative to most canonical "class A" 6.2 μm features as seen in the JWST H II PDR template (E. Peeters et al. 2002). This shift is consistent with border class B/class C PAH emission. Notably, the feature profile is broader in its red wing than HD 97300 (black line) and PDS 144N (green line). The spectrum of SR 21A (orange line), which is a T Tauri star with lower $T_{\rm eff}$, shows a similar PAH peak to that of T Cha. A major difference in the spectra of T Cha is that the component that peaks at 6.19 μm appears to be a weak feature along with the major peak at 6.27 μm. In all other spectra, the 6.2 μm region looks to be smooth and does not show additional components above the broad feature. Thus, we can say that T Cha has a minor class A component in its spectra, which peaks at 6.19 μm. The class A component is highlighted in Figure 5 (top panel).

Also, we see a 6.0 μm weak feature in all sources, which is proposed to be from C=O (carbonyl) stretching vibrations (E. Peeters et al. 2002) or olefinic C=C bonds (C.-H. Hsia et al. 2016). The 6.0/6.2 PAH ratio is higher in the case of the lower-temperature sources SR 21A and T Cha than for the other two stars and the H II PDR spectra. Figure 6 shows the variation of the 6.2 μm peak and 6.0/6.2 ratio with $T_{\rm eff}$ for T Cha and reference sources. The 6.0/6.2 ratio shows a decreasing trend with increasing $T_{\rm eff}$, indicating that hotter stars tend to exhibit lower values of this ratio, suggesting C=O (carbonyl) or olefinic C=C bonds. Stretching vibrational bonds tend to break in stronger UV fields and are dominant in lower UV fields.

[2] https://www.pdrs4all.org/

We see a systematic shift in the 6.2 μm peak position with spectral type, which further supports a correlation between PAH characteristics and the local stellar radiation environment. SR 21A and T Cha align within the class B domain but in the border region between class B and class C, whereas PDS 144N and HD 97300 have class B and class A type PAH features respectively. This also shows that with the decrease in UV hardness, the PAH class shifts from C to A (G. C. Sloan et al. 2007).

Overall, the 6.2 μm PAH feature in T Cha emerges as a border class B/class C feature linking the system more closely with circumstellar disks that harbor PAHs rather than with the class A type 6.2 μm band from H II region PDRs or reflection nebulae. It is interesting to note that the JWST spectrum of T Cha shows a class A pronounced feature peaking around 6.19 μm in the PAH complex.

3.5.2. 7.7 μm PAH Complex

The 7–9 μm region in intense PAH sources shows two major features at 7.7 and 8.6 μm. We analyze the 7.7 μm PAH band (or "7.7 complex") of T Cha and compare it with the reference spectra by dividing the 7.7 μm peak flux in the respective spectra. Figure 5 (middle) presents the resulting scaled profiles for spectra of T Cha and the reference sources. Each source shows a different PAH excitation environment, from high-mass stars with reflection nebulosity to lower-mass stars with protoplanetary disks.

For the H II PDR template, the spectrum displays a classical class A profile peaking near 7.6 μm with a steep-sided structure with a minor broad feature peaking at 7.8 μm, while HD 97300 shows a transitional "class AB" profile with comparable maxima at 7.6 and 7.8 μm. The Herbig Ae star PDS 144N exhibits a profile peaking at approximately 7.8 μm, consistent with class B emission, whereas the T Tauri star SR 21A presents a broader, redder feature characteristic of class C emission. Notably, the spectrum of T Cha is shifted to peak near ∼8.1 μm, which is a clear hallmark of a class C PAH spectrum; however, a minor subcomponent at 7.6 μm is also visible, which resembles the class A feature. This presence of a class A component in 6.2 and 7.7 μm PAHs is suggestive of a contribution from PAHs populated in a higher UV energy field than the stellar UV output. The minor class A component is highlighted in Figure 5 (middle panel). The dominant peak and broader red wing around 8.0–8.1 μm overwhelmingly classify T Cha's 7.7 μm band in the "class C" regime, parallel to what we find in its 6 μm emission.

A further point of interest is the weakness of the peak of the 8.6 μm band relative to the peak of the 7.7 μm band in T Cha. In all the reference sources, the peaks (relative height) at 7.7 and 8.6 μm are similar. The 7.7 μm band is attributed to C–C stretching modes, and 8.6 μm is attributed to C–H in-plane bending modes. PAHs with fewer peripheral hydrogen atoms will naturally have a weaker 8.6 μm feature. A possible proposition is that enhancement of the 6.0 μm feature, which is attributed to C=O (carbonyl) groups, could lead to a decrease in peripheral hydrogen atoms as it involves the removal of hydrogen atoms from the peripheral positions of the PAH structure. T Cha being the source with the lowest mass, it is possible that a higher level of hydrogen substitution might have occurred among the PAH population.

Overall, these observations reinforce the conclusion that T Cha hosts a distinctly shifted PAH spectrum consistent with a

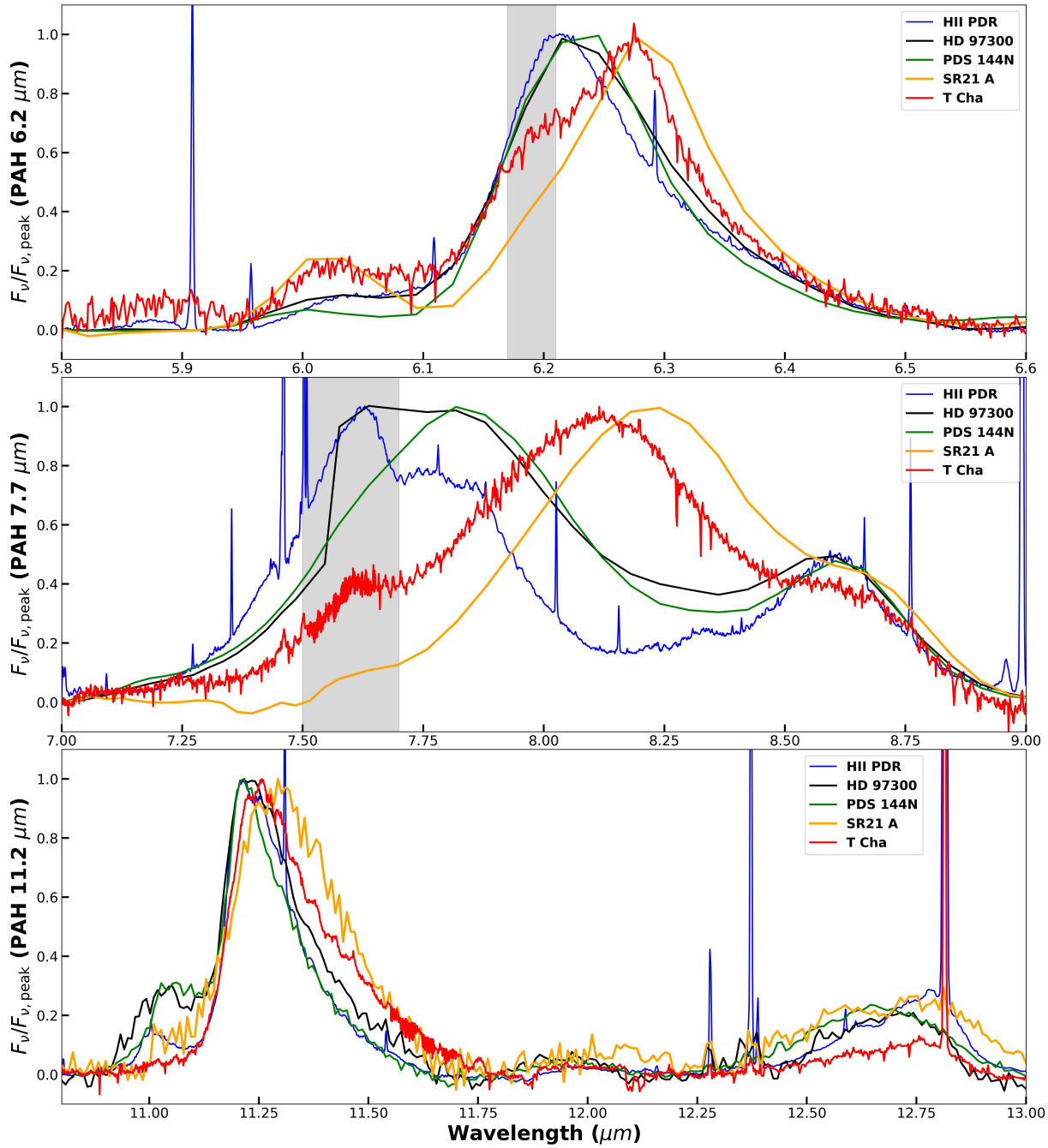

Figure 5. Composite figure showing continuum-subtracted, normalized PAH spectra from T Cha and four reference sources. Top panel (6.2 μm): spectra are normalized to unity at their 6.2 μm peak. Shown are the JWST H II PDR template (blue), HD 97300 (black), PDS 144N (green), SR 21A (orange), and T Cha (red). Middle panel (7.7 μm): the normalized spectra reveal variations in the 7.7 μm complex, with peak positions shifting from ∼7.6 μm in class A environments to ∼8.1 μm in T Cha, indicative of different PAH excitation conditions. Bottom panel (11.2 μm): the 11.2 μm feature, normalized similarly. The gray band highlights the minor class A feature identified in T Cha.

"class C" spectrum, while a weak subcomponent at 7.6 μm matches features from a more typical "class A" group, suggestive of multiple UV sources with varying hardness illuminating the disk of T Cha.

3.5.3. 11.2 and 12.7 μm PAH Features

We compared the spectra of T Cha with those of our reference sources in the 11–13 μm range after normalizing all profiles to unity at the 11.2 μm peak. In the H II PDR template, HD 97300, and PDS 144N, the 11.2 μm peak is centered at approximately 11.22 μm, and their overall profiles are nearly identical. In contrast, the 11.2 μm peak from T Cha is slightly redshifted to about 11.26 μm, while the spectrum of SR 21A exhibits the most redshifted peak at approximately 11.29 μm. These shifts, although present, are much smaller than those observed for the 6.2 and 7.7 μm C–C stretching modes.

Examination of the 11.0 μm feature reveals significant differences among the sources. Both HD 97300 and PDS 144N display a very pronounced 11.0 μm feature relative to the 11.2 μm emission, indicative of a PAH population with a high degree of ionization. The H II PDR spectrum also shows a

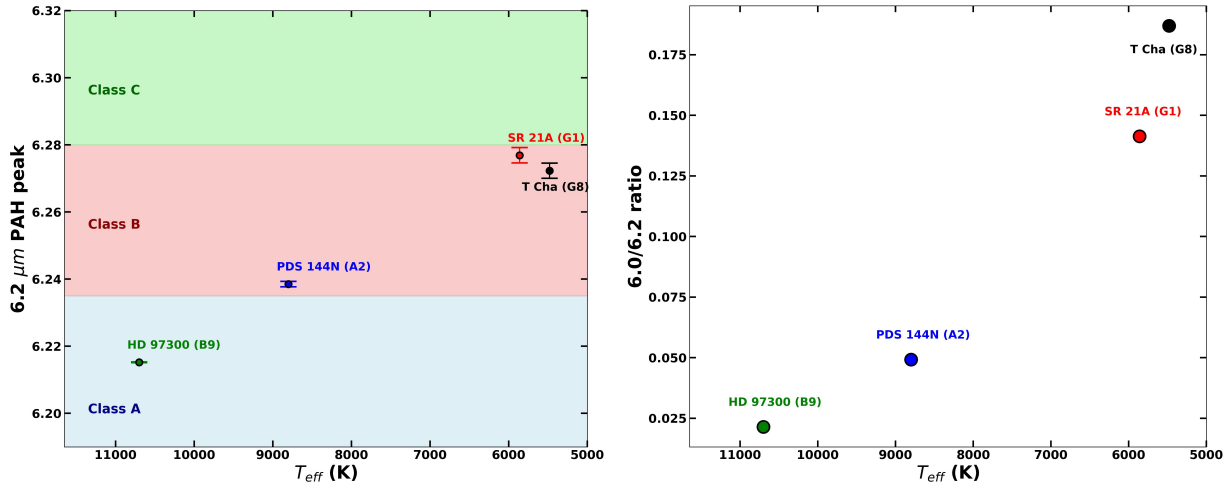

Figure 6. Variation of the 6.2 μm peak position (left) and the 6.0/6.2 ratio (right) with $T_{\rm eff}$ for T Cha and reference stars.

moderately strong 11.0 μm feature, whereas SR 21A exhibits only a weak bump at 11.0 μm, and T Cha shows no discernible 11.0 μm emission, suggesting that its PAHs are predominantly neutral.

Regarding the 12.7 μm feature, the relative fluxes are comparable among most sources, with the notable exception of T Cha. The 12.7 μm emission is relatively weak in T Cha, implying a lower abundance of duo or trio hydrogen modes within its PAH population (A. G. G. M. Tielens 2008). Also, a recent study by A. Ricca et al. (2024) shows that the 11.2 μm PAH is dominated by "zigzag PAHs," which have a high number of solo hydrogen atoms, and the 12.7 μm PAH is due to armchair edge PAHs. This behavior, when considered alongside the differences observed in the 11.0 μm feature, reinforces the conclusion that the PAHs in T Cha are mostly neutral and dominated by zigzag PAHs.

4. Discussion

4.1. Note on Radiation Hardness in T Cha

The observed line ratios such as [Ne III] 15.55/[Ne II] 12.81 $\approx$ 0.104 and [Ar III] 8.99/[Ar II] 6.98 $\approx$ 0.019 in the T Cha spectrum are low and clearly indicate a soft radiation field in its circumstellar environment (N. S. Bajaj et al. 2024). These low ratios indicate that very few photons above $\sim$40 eV (required for Ne^{3+} production) or above $\sim$28 eV (for Ar^{3+}) are present, implying that most of the neon and argon remains singly ionized. Furthermore, the detection of the H_2 S(3) line at 9.66 μm, together with the nondetection of the commonly observed hydrogen recombination line H I (7–6) at 12.37 μm (e.g., E. Rigliaco et al. 2015), reinforces this conclusion. In such a low-hardness regime, the incident photon energies are predominantly below 13.6 eV, ensuring that most of the PAH molecules remain neutral and that the UV field does not strongly influence their excitation. This is consistent with the expected spectral output of a G8 T Tauri star, where the radiation is softer than that found in high-excitation regions such as the Orion Bar or 30 Dor.

4.2. Charge and Size of the PAH Population

The model of charge and size of PAHs by A. Maragkoudakis et al. (2020) is applied to the PAH flux ratios of T Cha. The

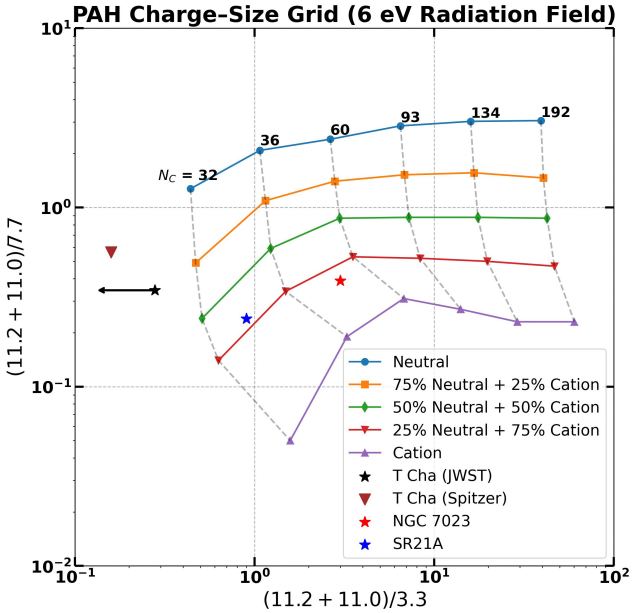

Figure 7. Location of T Cha observed by JWST (black star) and Spitzer (brown triangle) on the PAH charge–size diagnostic grid constructed using data from A. Maragkoudakis et al. (2020). The grid shows model tracks for PAH populations with varying neutral-to-cation ratios (colored curves), and dashed gray curves indicate PAH sizes. T Cha lies outside the model grid at both epochs, suggesting a low ionization fraction (75% neutral) and small PAH sizes, with $N_{\rm C} < 30$ based on extrapolation from the nearest model tracks.

model uses emission spectra of PAHs from the NASA Ames PAH IR Spectroscopic Database (PAHdb; A. L. Mattioda et al. 2020), accounting for a wide range of molecular sizes, structures, and charge states. We use the diagnostic grid in the (11.2 + 11.0)/7.7 versus (11.2 + 11.0)/3.3 flux ratio grid estimated using 6 eV photon energies, enabling simultaneous constraints on PAH ionization and size. The 3.3 μm PAH flux is obtained from VLT/ISAAC *L*-band spectra reported by V. C. Geers et al. (2007).

The charge–size grid incorporates synthetic spectra for varying neutral-to-cation fractions, allowing application to astrophysical sources with mixed PAH populations. In Figure 7, we present the location of T Cha on the PAH

charge–size grid generated under a 6 eV radiation field, using PAH fluxes from JWST and Spitzer. The position of T Cha lies distinctly outside the model grid in both ratios, in the lower left region of the diagram. C. J. Mackie et al. (2022) and A. K. Lemmens et al. (2023) reported that the 3.3 μm band flux in modeled PAH spectra used by A. Maragkoudakis et al. (2020) is systematically overestimated relative to the CH out-of-plane bending modes in the 10–15 μm range, by approximately 34%. To ensure a consistent comparison with these diagnostic grids, we scale our measured 11.2/3.3 μm ratios by a factor of 0.66 to account for the overestimation. The location of T Cha estimated using JWST and Spitzer in the grid suggests that the average PAH population in T Cha is characterized by low ionization (approximately 75% neutral) and small sizes, corresponding to $N_C < 30$ (where N_C is the number of carbon atoms) when extrapolating from the established PAH tracks. The finding of low ionization is consistent with the observation of N. S. Bajaj et al. (2024). The ratio estimated with Spitzer SL did not significantly move in the grid, suggestive of a very small change in ionization and size. One important point to consider is that the 3.3 μm PAH flux estimated from the *L*-band spectra was taken on 2006 April 18, and is used in both JWST and Spitzer ratios. The timeline of data matches better with the Spitzer epoch and is not at the wall destruction phase. So we assume that 3.3 μm should increase in the JWST epoch similar to 11.2 μm PAHs; the data point will move leftward horizontally, making this an upper limit on the *x*-axis. The figure also shows the reflection nebula NGC 7023 and the reference star SR 21A. NGC 7023 is illuminated by a B2 type star, and shows a higher value of N_C and is highly ionized (A. Maragkoudakis et al. 2020). The G2 type star SR 21A shows higher ionization and N_C than T Cha.

4.3. Origin of the Weak Class A PAH Subcomponent

The PAH spectrum of T Cha is dominated by a class C profile; however, detailed inspection of the 6.2 and 7.7 μm features reveals the presence of a weak subcomponent that peaks at approximately 6.19 μm and 7.6 μm, respectively. We propose that this subcomponent arises from a localized enhancement in the high-energy UV flux produced by disk accretion.

Transitional disks such as that of T Cha are characterized by a large inner dust gap (e.g., C. Espaillat et al. 2014). The reduction or removal of the inner dust wall not only exposes the outer disk to more stellar radiation but also permits UV photons from accretion hotspots to reach the disk surface. Magnetospheric accretion models predict that matter from the disk is funneled along magnetic field lines, forming shock-heated hotspots on the stellar surface with temperatures that can exceed 10,000 K (e.g., N. Calvet & E. Gullbring 1998). Although the underlying G8 stellar photosphere emits a relatively soft UV field that produces the predominant class C PAH emission, the localized hard UV excess from these hotspots can increase the ionization fraction of nearby PAH molecules.

The UVES observations by E. Cahill et al. (2019) reveal that the mass accretion rate in T Cha varies by more than an order of magnitude, from $\log(\dot{M}_{\rm acc}/M_\odot\ {\rm yr}^{-1}) \approx -8.8$ to -7.5. Such a significant increase in accretion rate would naturally lead to an enhancement in the accretion-driven UV excess hotspots, particularly in the far-ultraviolet regime. This elevated UV flux could locally harden the radiation field at the disk surface, especially while the inner wall is absent (C. Xie et al. 2025). We propose that during these high-accretion phases, the resulting burst of hard UV photons from the magnetospheric accretion hotspots is capable of transiently altering the ionization state of PAHs near the inner rim of the outer disk. This process could give rise to weak but detectable subcomponents in the PAH spectrum, including features peaking at ~6.19 μm and 7.6 μm, characteristic of class A profiles. The high resolution and sensitivity of JWST enabled the detection of these subcomponents in the two PAH features from the circumstellar disk for the first time. More such detections can enhance our knowledge on PAH excitation near multiple UV sources with varying hardness. To test this scenario, further observations could be directed at correlating accretion variability (tracked via UV excess or emission line diagnostics) with changes in the PAH feature ratios. T Cha presents a compelling science case for conducting a multi-epoch near- and mid-IR study.

5. Summary and Outlook

This study presents a detailed analysis of PAH emission in a transitional disk around the G8 T Tauri star, T Cha, using archival Spitzer data and recent JWST/MIRI MRS observations separated by nearly two decades. The disk has undergone a significant evolution in its structure, particularly the destruction of the inner dust wall, which revealed PAH emission features that had not previously been reported.

1. The continuum-subtracted Spitzer SL data of T Cha observed in 2005 showed 6.2, 7.7, and 8.6 μm PAH features, which were not reported before.
2. The relative flux of 6.2 μm PAH to 11.2 μm PAH is 0.77 ± 0.17 in the Spitzer epoch and 1.36 ± 0.02 in the JWST epoch; both values correspond to low ionization (approximately 75% neutral).
3. The 11.2 μm PAH band of T Cha has increased in flux by a factor of 3 in the 18 years between the Spitzer and JWST epochs but shows no change in profile shape or peak position, also indicating a stable, neutral PAH population despite variability in the UV field.
4. PAH band fluxes at 6.2, 7.7, 8.6, and 12.7 μm have increased at least twofold in the JWST epoch, resulting from increased UV excitation after destruction of the inner wall.
5. The 6.2 and 7.7 μm PAH bands show redshifted peaks and broad profiles consistent with class C spectra, which are commonly associated with low-UV environments and partially hydrogenated or aliphatic-rich PAHs.
6. Weak class A-like components at 6.19 and 7.6 μm suggest the presence of localized harder UV fields, possibly from accretion hotspots, contributing to a mixed PAH population.
7. The enhanced 6.0/6.2 PAH ratio of T Cha indicates higher carbonyl (C=O) substitution or increased olefinic C=C bonds compared to higher-mass sources.
8. The weaker 12.7/11.2 PAH ratio shows lower abundances of duo or trio hydrogen modes in the carbon chain, suggesting a "zigzag" molecular structure for PAHs in the disk of T Cha.
9. Using PAH diagnostic grids, the PAH population in T Cha is found to be predominantly neutral with small

carbon skeletons ($N_C < 30$), consistent with a soft UV radiation field from a G8-type star.

T Cha emerges as a benchmark system with persistent class C PAH emission and a class A subcomponent with pronounced variability in its inner disk continuum. Coordinated, triggerable multiepoch JWST observations based on photometric monitoring can directly test how radiation hardness and PAH charge respond across wall-high and wall-low phases and can help us understand changes in PAHs with accretion and disk variability.

Acknowledgments

Thanks to the referee for providing insightful comments and suggestions that significantly improved this paper. The author thanks Mr. Naman Bajaj for providing the JWST spectrum of T Cha. The JWST data used in this paper can be found in MAST: DOI: 10.17909/dhmh-fx64. Thanks to Dr. Vincent Geers for providing VLT/ISAAC spectra. Also, thanks to Dr. Shridharan Baskaran and Dr. Akhil Krishna R for their valuable comments on this work and wonderful discussions. The author thanks Dr. Merlin Thomas for the encouragement during this study. This work made use of Astropy:[3] a community-developed core Python package and an ecosystem of tools and resources for astronomy (Astropy Collaboration et al. 2013, 2018, 2022). Also, ChatGPT (OpenAI 2023) is used for assistance in correcting typos and grammar, though full responsibility for the manuscript's content remains our own.

Facilities: JWST (MIRI), Spitzer (IRS).

Software: astropy (Astropy Collaboration et al. 2013).

Author Contributions

The sole author was responsible for the conceptualization, data analysis, interpretation, software development, visualization, and writing of the manuscript.

Appendix A
Initial Gaussian Parameters of the 6.2 μm PAH Band

Table A1 gives the initial Gaussian parameters. The FWHM values are converted to standard deviations for the Levenberg–Marquardt fitter and bounds of ± 0.0025 μm are applied. The bound was set on mean values at ± 0.025 μm.

Table A1
Initial Gaussian Parameters for the 6 μm Region in T Cha

Component	Center (μm)	FWHM (μm)	Amplitude (erg s^{-1} cm^{-2} Å^{-1})
C1	6.01	0.067	1.5×10^{-16}
C2	6.075	0.080	1.5×10^{-16}
C3	6.20	0.080	4.0×10^{-16}
C4	6.29	0.095	6.0×10^{-16}
C5	6.39	0.135	1.5×10^{-16}
C6	6.50	0.062	1.5×10^{-16}

Appendix B
Integrating PAH Fluxes

Figures B1 and B2 show the flux estimation through integration of PAH wavelength regions detailed in Section 3.2.3 for JWST, Spitzer, and VLT/ISAAC.

[3] http://www.astropy.org

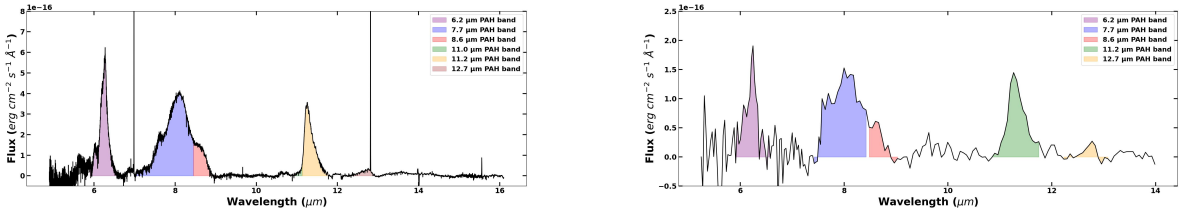

Figure B1. Continuum-subtracted JWST/MIRI (left panel) and Spitzer (right panel) spectra of T Cha highlighted with integrated PAH regions. The final flux in the 12.7 μm PAH band is estimated after the subtraction of fitted [Ne II] flux in the case of the JWST spectrum.

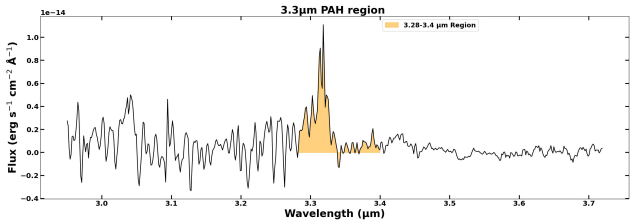

Figure B2. Continuum-subtracted ISAAC *L*-band spectrum of T Cha highlighting 3.3 μm integrated PAH regions taken from V. C. Geers et al. (2007).

References

Arun, R., Mathew, B., Manoj, P., et al. 2023, MNRAS, 523, 1601
Arun, R., Mathew, B., Shridharan, B., et al. 2025, RAA, 25, 095005
Astropy Collaboration, Price-Whelan, A. M., Lim, P. L., et al. 2022, ApJ, 935, 167
Astropy Collaboration, Price-Whelan, A. M., Sipőcz, B. M., et al. 2018, AJ, 156, 123
Astropy Collaboration, Robitaille, T. P., Tollerud, E. J., et al. 2013, A&A, 558, A33
Bajaj, N. S., Pascucci, I., Gorti, U., et al. 2024, AJ, 167, 127
Bauschlicher, C. W., Jr., Peeters, E., & Allamandola, L. J. 2008, ApJ, 678, 316
Brown, J. M., Blake, G. A., Dullemond, C. P., et al. 2007, ApJL, 664, L107
Cahill, E., Whelan, E. T., Huélamo, N., & Alcalá, J. 2019, MNRAS, 484, 4315
Calvet, N., & Gullbring, E. 1998, ApJ, 509, 802
Chown, R., Sidhu, A., Peeters, E., et al. 2024, A&A, 685, A75
Ercolano, B., & Pascucci, I. 2017, RSOS, 4, 170114
Espaillat, C., Furlan, E., D'Alessio, P., et al. 2011, ApJ, 728, 49
Espaillat, C., Muzerolle, J., Najita, J., et al. 2014, in Protostars and Planets VI, ed. H. Beuther et al. (Tucson, AZ: Univ. Arizona Press), 497
Espaillat, C. C., Thanathibodee, T., Zhu, Z., et al. 2024, ApJL, 973, L16
Fernández, D., Figueras, F., & Torra, J. 2008, A&A, 480, 735
Flaherty, K., Muzerolle, J., Rieke, G., et al. 2012, ApJ, 748, 71
Geers, V. C., Augereau, J. C., Pontoppidan, K. M., et al. 2006, A&A, 459, 545
Geers, V. C., van Dishoeck, E. F., Visser, R., et al. 2007, A&A, 476, 279
Hony, S., Van Kerckhoven, C., Peeters, E., et al. 2001, A&A, 370, 1030
Hsia, C.-H., Sadjadi, S., Zhang, Y., & Kwok, S. 2016, ApJ, 832, 213
Huélamo, N., de Gregorio-Monsalvo, I., Macias, E., et al. 2015, A&A, 575, L5
Kessler-Silacci, J., Augereau, J.-C., Dullemond, C. P., et al. 2006, ApJ, 639, 275
Lahuis, F., van Dishoeck, E. F., Blake, G. A., et al. 2007, ApJ, 665, 492
Lebouteiller, V. 2023, arXiv:2309.06876
Lebouteiller, V., Barry, D. J., Goes, C., et al. 2015, ApJS, 218, 21
Lebouteiller, V., Barry, D. J., Spoon, H. W. W., et al. 2011, ApJS, 196, 8
Lemmens, A. K., Mackie, C. J., Candian, A., et al. 2023, FaDi, 245, 380
Mackie, C. J., Candian, A., Lee, T. J., & Tielens, A. G. G. M. 2022, JPCA, 126, 3198
Manoj, P., Kim, K. H., Furlan, E., et al. 2011, ApJS, 193, 11
Maragkoudakis, A., Peeters, E., & Ricca, A. 2020, MNRAS, 494, 642
Matsuura, M., Bernard-Salas, J., Lloyd Evans, T., et al. 2014, MNRAS, 439, 1472
Mattioda, A. L., Hudgins, D. M., Boersma, C., et al. 2020, ApJS, 251, 22
Muzerolle, J., Flaherty, K., Balog, Z., et al. 2009, ApJL, 704, L15
Olofsson, J., Benisty, M., Le Bouquin, J.-B., et al. 2013, A&A, 552, A4
Owen, J. E. 2016, PASA, 33, e005
Peeters, E., Habart, E., Berné, O., et al. 2024, A&A, 685, A74
Peeters, E., Hony, S., Van Kerckhoven, C., et al. 2002, A&A, 390, 1089
Perrin, M. D., Duchêne, G., Kalas, P., & Graham, J. R. 2006, ApJ, 645, 1272
Pohl, A., Sissa, E., Langlois, M., et al. 2017, A&A, 605, A34
Ricca, A., Roser, J. E., Boersma, C., Peeters, E., & Maragkoudakis, A. 2024, ApJ, 968, 128
Rigliaco, E., Pascucci, I., Duchene, G., et al. 2015, ApJ, 801, 31
Schisano, E., Covino, E., Alcalá, J., et al. 2009, A&A, 501, 1013
Sellek, A. D., Bajaj, N. S., Pascucci, I., et al. 2024, AJ, 167, 223
Seok, J. Y., & Li, A. 2017, ApJ, 835, 291
Sloan, G. C., Jura, M., Duley, W. W., et al. 2007, ApJ, 664, 1144
Tielens, A. G. G. M. 2008, ARA&A, 46, 289
Tielens, A. G. G. M. 2011, EAS Publ. Ser., 46, 3
van Diedenhoven, B., Peeters, E., Van Kerckhoven, C., et al. 2004, ApJ, 611, 928
Xie, C., Pascucci, I., Deng, D., et al. 2025, ApJ, 978, 34